Comparison of magnetic islands stabilization strategies from Magneto-Hydro-Dynamic simulations

Olivier Février, Patrick Maget, Hinrich Lütjens, Peter Beyer

Comparison of magnetic islands stabilization strategies from Magneto-Hydro-Dynamic simulations

O. Février[1], P. Maget[1], H. Lütjens[2], P. Beyer[3] [1]CEA, IRFM, F-13108 Saint Paul-lez-Durance, France. [2]Centre de Physique Théorique, Ecole Polytechnique, CNRS, France. [3]Aix-Marseille Université, CNRS, PIIM UMR 7345, 13397 Marseille Cedex 20, France.

Correspondance: `patrick.maget@cea.fr`

Abstract

The degradation of plasma confinement in tokamaks by magnetic islands motivates to better understand their possible suppression using Electron Cyclotron Current Drive (ECCD) and to investigate the various strategies relevant for this purpose. In this work, we evaluate the efficiency of several control methods through nonlinear simulations of this process with the toroidal MHD code XTOR Lütjens and Luciani (2010), which has been extended to incorporate in Ohm's law a source term modeling the RF driven current resulting from the interaction of the RF waves with the plasma. A basic control system has been implemented in the code, allowing testing advanced strategies that require feedback on island position or phase. We focus in particular on the robustness of the control strategies towards the uncertainties that apply on the control and ECCD systems, such as the risk of misalignment of the current deposition or the possible inability to generate narrow current deposition.

1 Introduction

Magnetic islands can grow into the plasma and lead to a degradation of the confinement. It is however well-known that they can be controlled and suppressed by driving current inside them using ECCD (Electron Cyclotron Current Drive) Maraschek (2012), with several candidate strategies to routinely suppress islands in future tokamaks. The simplest form of island control consists in applying continuous ECCD on the expected location of the affected rational surface. While rotating, the island O-Points and X-points will successively cross the current deposition, and the mean effect will be stabilizing. This however requires being able to target precisely the rational surface, adding constraints on the equilibrium reconstruction and ECCD launchers alignment. Since misalignment may lead to a reduction of the control performances, or even to a greater destabilization of the mode, control schemes must be adapted in order to be robust towards possible misalignment issues. While a possible solution is to use feedback on the mode amplitude to ensure that current deposition is done at the right position, simpler strategies are explored in order to design robust, albeit efficient, control system. One of these methods consists of sweeping the ECCD deposition around the estimated radial position of the mode. This strategy has been successfully tested on TCV Felici et al. (2012) and applied to ASDEX-Upgrade and TCV during the 2014 and 2015 MST-1 campaigns. It relies on the fact that the mean effect will still be favorable for the mode reduction, at the cost of a theoretical lower efficiency than direct –and precise– targeting of the island, but relieving the constraint of precise radial localization of the mode. Another pitfall is the

width of the ECCD deposition. Larger deposition (with respect to the island width) have a lower efficiency, thus encouraging to optimize the ECCD design for a narrow deposition or, more precisely, to enhance the ratio I_{RF}/δ_{RF}^2 Pletzer and Perkins (1999) or I_{RF}/δ_{RF} Hamamatsu and Fukuyama (2000), where I_{RF} is the current deposited by the ECCD system and δ_{RF} the width of this deposition. However, it has been observed experimentally Harvey et al. (2002); Coda et al. (2003); Kirov et al. (2002) that the deposition can actually be larger than expected from ECCD/ECRH modeling. This can be due to cross-field diffusion of the fast electrons density (constituting the EC current), for instance because of turbulence on the deposition location, leading to a broadening of the driven current density deposition and therefore to a reduction in the maximum driven current density Giruzzi and Fidone (1989); Giruzzi (1993); Coda et al. (2006); Bertelli and Westerhof (2009); Bertelli et al. (2010). It has also been shown that the electron density fluctuations near the plasma edge, or along the path of the RF-waves, might lead to a broadening of the current deposition as well as a fluctuating power deposition profile Tsironis et al. (2009); Peysson et al. (2011); Decker, J. et al. (2012). In ITER, the local micro-turbulence impact should be negligible and will not significantly increase the current width Casson et al. (2015), but effects of edge turbulence on wave propagation might enlarge considerably the EC deposition, up to a factor 2 Tsironis et al. (2009); Peysson et al. (2011); Decker, J. et al. (2012); Sysoeva et al. (2015). As these effects are difficult to control, it is necessary to design control strategies that are able to overcome them. In this article, we explore and compare these different methods of control. In a first part, we present the equilibrium and MHD model used for the modeling. We start by presenting the preemption, that consist in trying to avoid the islands in the first place, thanks to a preventive strike on the rational surface susceptible to be plagued by magnetic islands. The results obtained with XTOR are compared with analytical work Pletzer and Perkins (1999). We then proceed to compare different control schemes that can be used in the case of an existing island in the plasma, in light of the different difficulties that must be overcome: first, the possible misalignment, and then, the possible large deposition width. We then synthesize those results, defining a gain function G that allows to quickly compare different control strategies.

2 Framework of the simulation

2.1 Equilibrium used in the simulations

We construct a circular cross-section magnetic equilibrium, using the Grad-Shafranov code CHEASE Lütjens et al. (1996). The inverse aspect ratio is $\epsilon = 0.3$ and the major radius $R_0 = 2.4m$, while the pressure profile is given by $\partial_\psi p \propto (1-\psi)$ and the current density profile by $I^* \propto (1-\psi)^2$. The central magnetic field is $B_0 = 3$ T, the ion density $n_i(0) = 2 \times 10^{19}$ m^{-3}, electron temperature $T_e(0) = 3910$ eV, and $\tau \equiv T_i/T_e = 1$. The position of $q = 2$ is prescribed at $\rho = \sqrt{\psi} = 0.5$, ρ being the normalized poloidal flux unit. This corresponds to $x \equiv r/a = \sqrt{\Phi} \approx 0.34$, where Φ is the normalized toroidal flux. The density profile is defined as

$$N(\psi) = \frac{n_i(\psi)}{n_i(0)} = \frac{1 - 0.32\psi}{1 + 0.1\psi^4} \tag{1}$$

2.2 Single-fluid MHD Model

We use the single-fluid model of the nonlinear 3D full-MHD code XTOR-2FLütjens and Luciani (2010). The equations solved are, in normalized units:

$$\left(\partial_t + \mathbf{V}\cdot\nabla\right) N + N\nabla\cdot\mathbf{V} + \nabla\cdot\Gamma_{turb} = S \quad (2)$$

$$N\left(\partial_t\mathbf{V} + \mathbf{V}\cdot\nabla\mathbf{V}\right) - \mathbf{J}\times\mathbf{B} + \nabla p = \nu\nabla^2\mathbf{V} \quad (3)$$

$$\mathbf{E} + \mathbf{V}\times\mathbf{B} - \eta\left(\mathbf{J} - \mathbf{J_{CD}} - J_{RF}\frac{\mathbf{B}}{|\mathbf{B}|}\right) = 0 \quad (4)$$

$$\partial_t\mathbf{B} = -\nabla\times\mathbf{E} \quad (5)$$

$$\left(\partial_t + \mathbf{V}\cdot\nabla\right) p + \Gamma p\nabla\cdot\mathbf{V} = \frac{2}{3}\left\{H - \nabla\cdot\mathbf{q}^{\chi}\right\} \quad (6)$$

$$\frac{\partial J_{RF}}{\partial t} = \nu_f\left(J^s_{RF} - J_{RF}\right) + \chi^{RF}_{\perp}\nabla^2_{\perp}J_{RF} + \chi^{RF}_{||}\nabla^2_{||}J_{RF} \quad (7)$$

$\mathbf{V} = \mathbf{V_E} + \mathbf{V_{||i}}$. $\mathbf{J_{CD}}$ is a current source intended to restore the equilibrium current profile, and is defined as $\mathbf{J_{CD}} = \mathbf{J}|_{t=0}$, The ratio of specific heat is $\Gamma = 5/3$, H is the heat source, which restores the equilibrium pressure profile. The heat flux q^{χ} is defined as $q^{\chi} = -N\chi_{||}\nabla_{||}T - N\chi_{\perp}\nabla_{\perp}T$, where $T = p/N$ and $\chi_{||}$ and $\chi_{\perp}$ diffusion coefficients accounting for the parallel and perpendicular transport. $\chi_{\perp}$ is chosen such that $\chi_{\perp}/\eta = 150$, and $\chi_{||}$ is chosen such that $\chi_{||}/\chi_{\perp} = 10^8$. The Lundquist number is $S = 10^7$. The time is rescaled so that $t[s] = S_r\tau_A t_{XTOR}$ where $\tau_A = 2.32\times10^{-7}s$ is the Alfvén timescale and $S_r = 75 = S_{real}/S_{simulation}$. The magnetic Prandtl number is set to Prm $= \nu/\eta = 10$. Discretization in the radial direction is done using finite differences, with a resolution of 512 points, while description in the poloidal and toroidal direction is achieved using Fourier decomposition, with a a resolution of 64 in the poloidal direction and 16 in the toroidal direction, thus enabling the description of the $n = 0, 1, 2, 3, 4$ modes, while avoiding aliasing problems. The implementation of the ECCD source-term is detailed in Février et al. (2016). The source term J^s_{RF} that appears in equation 7 can either be specified to be 1D or 3D. In the first case, it is specified as in equation 8 :

$$J^s_{RF}\left(\rho,\theta,\varphi\right) = J^{s,0}_{RF}\times \mathrm{e}^{-\frac{\left(\rho-\rho_{RF}(t)\right)^2}{2\sigma^2_{\rho}}} \quad (8)$$

It corresponds to the case where the 3D nature of the current deposition does not matter, which is the case when the island rotation period is small compared to the characteristic island growth time. In the following simulations, we use two different values for σ_ρ, that we will refer as "thin" and "broad" which corresponds respectively to $\delta_{RF}/W_{sat} \approx 0.7$ and $\delta_{RF}/W_{sat} \approx 1.4$, where δ_{RF} is the full-width at half-value of the current deposition after broadening by perpendicular diffusion ($\chi^{RF}_{\perp}$ contribution in equation 7). The modeling of the modulation process requires however to represent the current deposition as a toroidally and poloidally localized current density, so as to account for the localized nature of the plasma-wave interaction, leading to a specific expression for J^s_{RF}. As in our resistive test case, the island rotation is negligible, thus preventing the use of modulation, we add an artificial rotation of the source term, which mimics the rotation of the plasma with respect to the current deposition, so that $\varphi_{RF}(t) = \varphi_{RF,0} + \omega_\varphi t$. The source term J^s_{RF} then writes

$$J^s_{RF}\left(\rho,\theta,\varphi\right) = J^{s,0}_{RF}(t)\times \mathrm{e}^{-\frac{\left(\rho-\rho_{RF}(t)\right)^2}{2\sigma^2_{\rho}}}\,\mathrm{e}^{-\frac{\left(\theta-\theta_{RF,0}\right)^2}{2\sigma^2_{\theta}}}\,\mathrm{e}^{-\frac{\left(\varphi-\varphi_{RF}(t)\right)^2}{2\sigma^2_{\varphi}}} \quad (9)$$

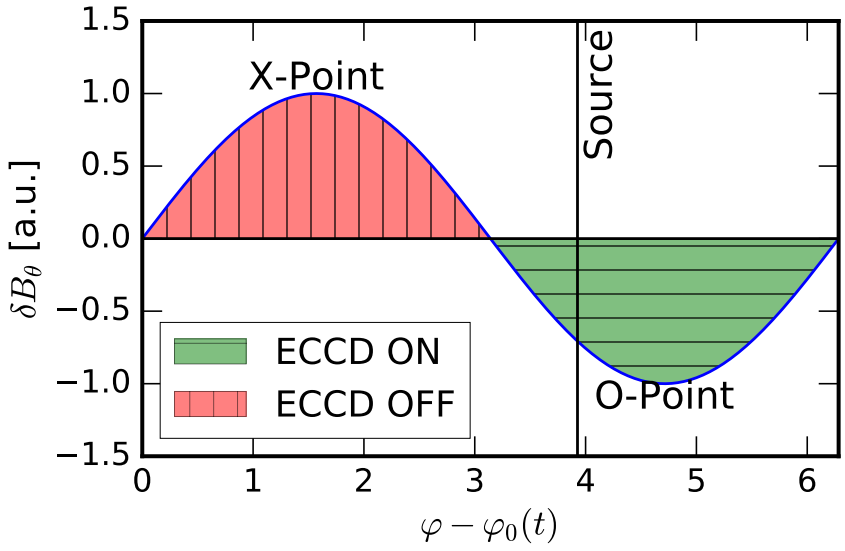

Figure 1: (2,1) poloidal perturbation δB_θ as seen by the control system, monitoring the value of B_θ on $\rho = 1$, edge of the plasma in XTOR-2F. The duty-cycle is set to 50%, and the green color indicates positions where the source is switched on, while red color indicate position where the source is switched off, as X-Point is facing the current deposition location.

Through this whole article, the RF current is taken to be $I_{RF}/I_P = 1\%$. In order to test the principle of the modulation, which requires feedback on what is happening inside the plasma, a basic "plasma control system" has been added in XTOR, allowing to detect the presence of an island by measuring, at the edge of the plasma, the perturbation of the poloidal component magnetic field $\tilde{B}_\theta$ along the toroidal direction. Note that we chose for simplicity to measure the perturbation along the whole torus in the toroidal direction, which is roughly equivalent to measuring only at a certain position in the toroidal direction, but along the time, taking advantage of the toroidal rotation. The toroidal mode number of the dominant mode is detected (in our case $n = 1$) and it is assumed that $m = n + 1$. On figure 1 is plotted the $n = 1$ poloidal perturbation δB_θ of the magnetic field as seen by the controller. On the simulations presented here, the controller considers that the source is facing an O-Point when $\delta B_\theta \leq 0$, corresponding to a modulation with a 50% duty-cycle.

2.3 Island dynamics

The dynamics of the magnetic island can be modeled by the Modified Rutherford equation (MRE) Sauter (2004)

$$\frac{\mathrm{d}W}{\mathrm{d}t^\star} = a\Delta' + \sum \Delta_i(W) \tag{10}$$

where $\Delta_i(W)$ is a generic notation to describe the contributions of different physical effects on the island width evolution. In particular, the impact of the ECCD on the island dynamics can be modeled by a supplemental term Δ_{RF} Hegna and Callen (1997) defined as

$$\Delta_{RF} = -\frac{16}{\pi}\frac{\mu_0 R_0}{s\psi'_s} I_{RF} \frac{1}{W^2} \eta_{RF} \tag{11}$$

In equation 11, η_{RF} is the *efficiency* Hegna and Callen (1997), that defines how efficient the RF current is in stabilizing the island. If $\eta_{RF} > 0$, the co-current ECCD is stabilizing, while $\eta_{RF} < 0$ leads to mode destabilization. In addition to η_{RF}, we introduce the correlation between the toroidal current perturbation δJ_ϕ and the RF current δJ_{RF}. As the role of the latter is to compensate the former, these two quantities should be anti-correlated (that is, $\delta J_\phi = -J_{RF}$) when stabilizing. We define the (anti-)correlation of these two quantities as

$$R_J\left(J_{RF}\right) = -\frac{\int \mathrm{d}V \delta J_\phi J_{RF}}{\left(\int \mathrm{d}V \delta J_\phi^2\right)^{\frac{1}{2}} \left(\int \mathrm{d}V J_{RF}^2\right)^{\frac{1}{2}}} \tag{12}$$

$R_J\left(J_{RF}\right)$ quantifies how well the RF current is able to counterbalance the toroidal current perturbation, in a similar fashion to the efficiency η_{RF}. Its value is positive when the RF current is shaped so as to compensate the island current, the maximum (1) being reached when the RF current compensate exactly the current perturbation δJ_ϕ. It goes to negative values when the injected current density leads to an increase of the island current. $R_J\left(J_{RF}\right)$ has the advantage of being easily computed within the framework of our 3D MHD simulations, for which the reduction of the 3D results to 0D quantities such as W or η_{RF} is not straightforward.

3 Preemption

3.1 Impact of preemption on mode stability and growth rate

A possible solution to control the tearing modes is to prevent their apparition in the first place, which can be achieved by tailoring the current profile so as to increase the linear stability of the mode Glasser et al. (1977); Pletzer and Perkins (1999). Moreover, computations show that the contribution of Δ_{RF} is non-null, and stabilizing, even in the absence of an island Hegna and Callen (1997); Westerhof et al. (2016). The stability of the mode is evaluated in two ways. First, we compute the cylindrical stability index Δ' Furth et al. (1973) (in this section, Δ' denotes the stability parameter of the (2,1) mode $\Delta'_{(2,1)}$), and second we determine the linear growth rate of the (2,1) mode from the evolution of its magnetic energy. On figure 2, the evolution of the Δ' for a source of given width ($\sigma_\rho = 0.025$, $\chi_\perp^{RF}/\chi_\perp = 60\%$), centered on the resonance surface, is plotted as a function of the injected ECCD current. On figure 2 we have also plotted the growth rate $\gamma_{(2,1)}$ of an initially unstable $(2,1)$-tearing mode, in two cases. In both cases, we start the simulation by letting the $n = 0$ components of the fields ($\mathbf{V}$,$\mathbf{B}$, p, N) evolve under the action of the ECCD

current deposition. Once a new equilibrium has been reached, we proceed in two ways:

- In the "No-current case", we modify the term $\mathbf{J_{CD}}$ that appears in XTOR's Ohm's law to reflect the new equilibrium value of $\mathbf{J}$, and we set $J_{RF} = 0$. We then add a perturbation to the system and observe its growth or decay. We therefore see the evolution of a perturbation under the action of the purely equilibrium contribution from the RF current density, that is, its action on the Δ'.
- In the "With current case", we keep J_{RF} as it is, do not modify $\mathbf{J_{CD}}$, and add a perturbation. This allows us not only to evaluate the effect of the RF current deposition on equilibrium, but also the contribution from its $n \neq 0$ harmonics.

One can see that for both cases, for sufficient current, the mode is indeed stabilized. One can also notice that it is not necessary to reach $\Delta' < 0$ to have an effective stabilization of the mode. Indeed, the curvature stabilization Glasser et al. (1975); Kotschenreuther et al. (1985); Lütjens et al. (2001) also plays a stabilizing role. The "with current case" appears as more stabilizing, as the contribution from the RF-current $n \neq 0$ harmonics is known to have a stabilizing effects Westerhof et al. (2016), thus explaining why this case is more stabilizing than the "No-current case". On figure 2, bottom panel, we also have plotted the saturation width of a (2,1) seed island corresponding to the "No-current case", that is, the equilibrium modified by the ECCD deposition, the latter being then removed. We observe a quick drop of the saturation width as Δ' is decreased, which is expected from equation 10. We observe that the saturation width goes to 0 for $I_{RF}/I_P \approx 1.5\%$, while at $I_{RF}/I_P = 1\%$, the saturation width is about 3%, a similar width to what we found in section 4 in the case of control of a pre-existing island, thus indicating that in our particular case, preemption and island suppression require roughly the same level of power, in contrast with experimental results on DIII-D and TCV Haye (2006); Felici et al. (2012); Kolemen et al. (2014). This difference can be explained by the fact that we do not consider the bootstrap current in our simulations.

3.2 On the dependence of preemption efficiency on source width and location

The equilibrium modification induced by the ECCD will be dependent on the source width and location. In Pletzer and Perkins (1999), it is shown that the modification of Δ' can be roughly evaluated by equation 13 (see Pletzer and Perkins (1999) for the definition of $h(\alpha)$ and a figure representing it). Note that in this subsection, we use preferentially the normalized toroidal flux unit x. $\chi_\perp^{RF}$ is set to 0 so as to ensure total control on source shape and width.

$$\Delta' \approx -\frac{4\sqrt{\pi}}{s\sqrt{2}\sigma_x}\left(\frac{J_{RF}^s}{j_q}\right)h(\alpha) \tag{13}$$

where $j_q = 2B_\varphi/Rq_s$ and $\alpha = (x_{RF} - x_s)/\sqrt{2}\sigma_x$ (x_s is the radial position of the resonant surface. See equation 14 for a definition of x_{RF} and σ_x). α quantifies

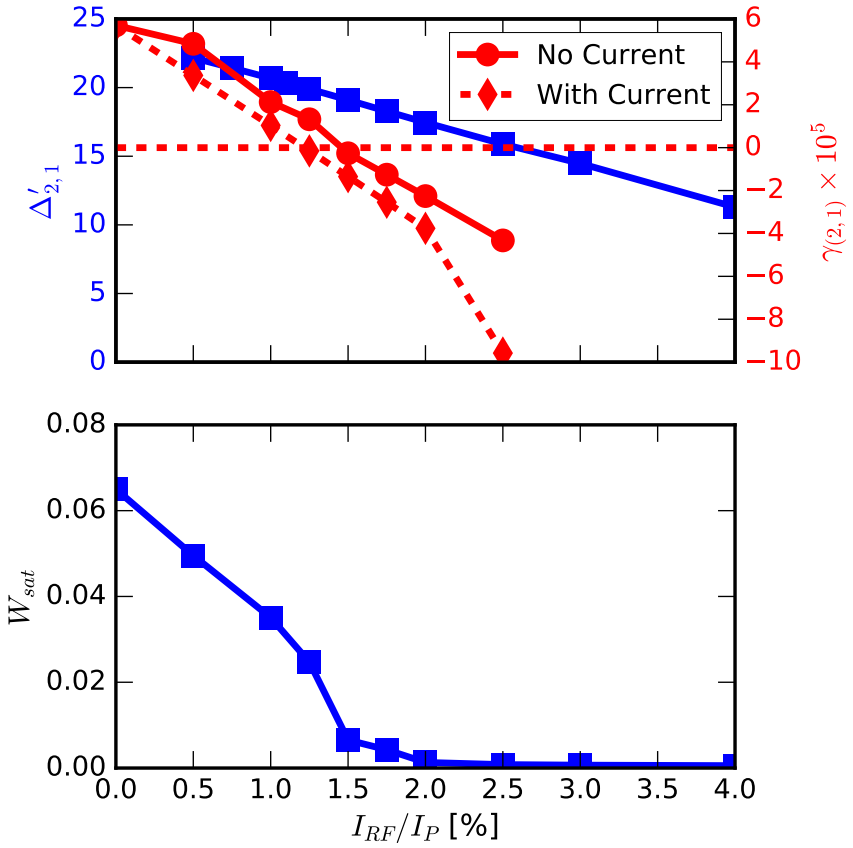

Figure 2: Top panel: evolution of Δ' for the (2,1)-mode as a function of the total injected current for a deposition centered on $\rho_{q=2}$. The scaling is in line with analytical predictions by Pletzer Pletzer and Perkins (1999), where a linear scaling is expected (see equation 13). Bottom panel: Evolution of the saturation width of a (2,1) seed island for the equilibrium modified by the ECCD deposition. J_{CD} has been modified to reflect the equilibrium current profile modification, while the RF contribution of the Ohm's law has been shut down, allowing to discriminate the equilibrium effects from the non-equilibrium ones.

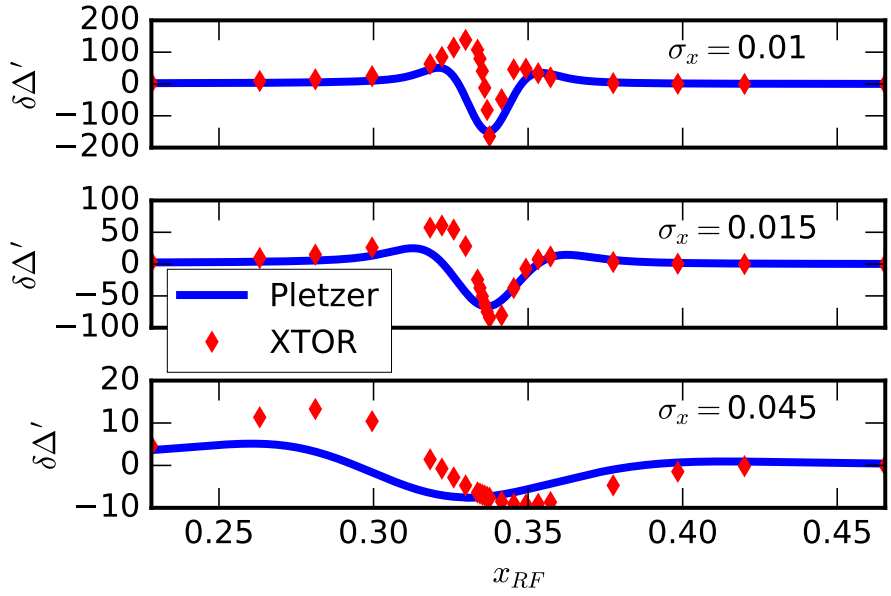

Figure 3: Comparison of the variation of Δ', $\delta\Delta'$, as given by equation 13, and as computed by XTOR, as a function of source radial misalignment for different source widths (quantified by the values of σ_x^2).

the distance of the RF current density peak to the resonant surface. The current source term is defined as

$$J^s_{RF}(r,\theta,\varphi) = J^{s,0}_{RF} \times \mathrm{e}^{-\frac{(x-x_{RF})^2}{2\sigma_x^2}} \tag{14}$$

On figure 3, the modification of the Δ', $\delta\Delta'$, obtained with XTOR is plotted against the values expected from equation 13, as a function of misalignment for different source widths (quantified by the values of σ_x^2). While the results obtained with XTOR are in qualitative agreement with equation 13, especially in the limit of a thin source ($\sigma_x = 10^{-2}$) and in the outside vicinity of the rational flux surfaces, quantitative discrepancies remain for the magnitude of $\delta\Delta'$. Moreover, XTOR seems to predict more abrupt variations of Δ', with a transition region much narrowly localized in the vicinity of the resonance than computed analytically. These differences could be partly explained by the approximations made to derive 13.

3.3 Mitigating radial misalignment issues while preempting: sweeping of the deposition

Because of uncertainties on equilibrium reconstruction and possible systematic errors in the ECRH/ECCD system (be it on the deposition location real-time computation or the mirrors alignment), it might be complicated to target precisely the mode radial position, which, as we have seen, might severely impact the efficiency of the preemption. To avoid this pitfall, one can envision sweeping

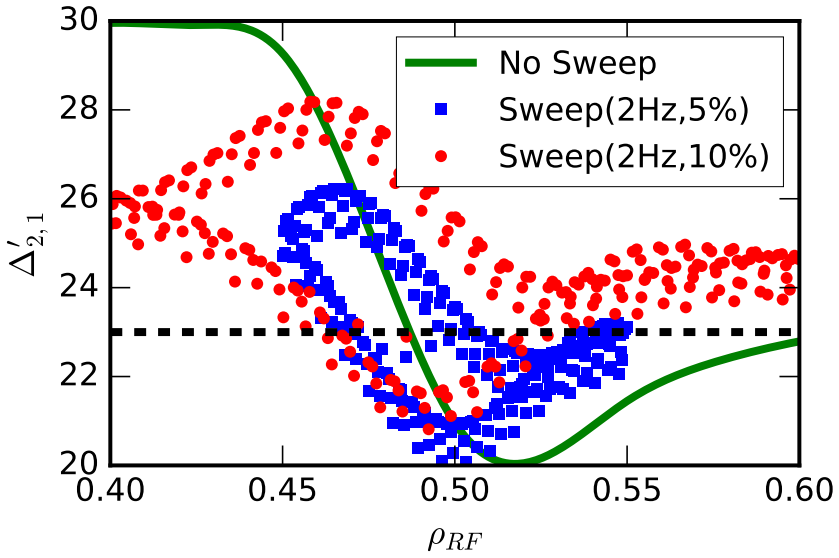

Figure 4: Impact of sweeping amplitude on the Δ' evolution, plotted as a function $\rho_{RF}(t)$. Reducing the amplitude of the sweep permits to stay confined in the vicinity of the rational surface, where the preemption is more efficient. The mean value of Δ' gets lower as amplitude is increased. The black dotted line indicates the initial Δ' in absence of sweeping.

the radial position of the ECCD around the rational flux surface estimated position, so as to ensure that current will have in average a favorable effect. This has been successfully done on TCV and Asdex-Upgrade, but the question of the efficiency of this process, which can be expected to be lower than direct, and precise, targeting, remains. Indeed, sweeping occurs on typical scales of a few Hz, and it may be slow enough to lead to a complex dynamics of Δ', passages across destabilizing areas being susceptible to increase -temporarily-significantly the Δ', thus leading to mode destabilization (or diminution of critical width in the case of a metastable mode). We have plotted on figure 4 the impact of the sweeping process on the Δ' for two sweeping amplitudes, the frequency being set to 2 Hz. On figure 5, we have represented the role of the frequency on the Δ' dynamics, for a given sweep amplitude (10%). One can see that increasing the sweeping frequency lead to lower excursion of Δ' around its mean value, and thus the mode is less destabilized. One should however note than in real tokamak applications, the maximum achievable frequency will be constrained by the EC system. An interesting behavior of Δ' can be seen on figures 4 and 5: the sweeping process induces a hysteresis-like modification of the equilibrium, due to the finite timescale necessary for the current profile, and therefore mode stability, to be affected by the EC deposition. This behavior can be modeled by a simple analytical model to reproduce this result, described in (equation 15), where $\rho_{RF}(t) = \rho_{RF,0} + A \times \text{triangle}_f(t)$ correspond to the sweeping, centered on $\rho_{RF,0}$ and of amplitude A, while triangle_f is a triangle wave function of given

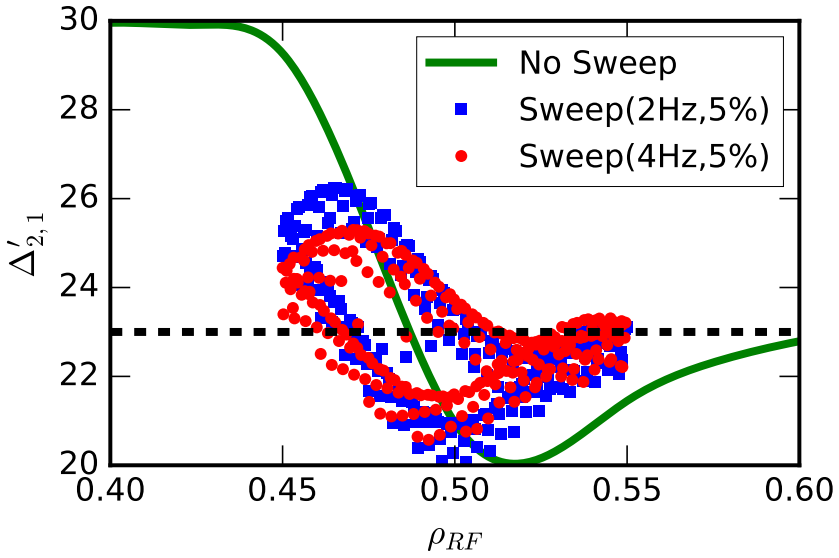

Figure 5: Impact of sweeping frequency on the Δ' evolution, plotted as a function $\rho_{RF}(t)$. Increasing the sweeping frequency lead to lower excursion of Δ' around its mean value, thus limiting the possible deleterious effect of sweeping when located inside the rational surface position. The black dotted line indicates the initial Δ' in absence of sweeping.

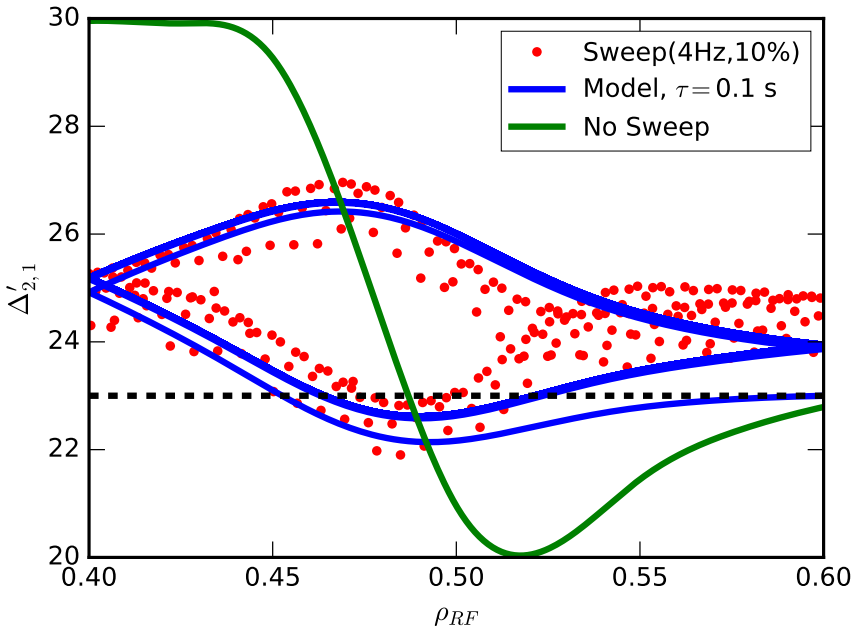

Figure 6: Evolution of Δ' produced by the analytical model (equation 15), compared to results obtained XTOR in case of a sweep of amplitude $A = 0.05$ and frequency $f = 4$ Hz. τ has been set to 0.1 s. The black dotted line indicates the initial Δ' in absence of sweeping.

frequency f. $\Delta'_s(\rho_{RF})$ denotes the final value of Δ' for a source at fixed position ρ_{RF}, and τ the typical timescale needed for the RF current to impact the plasma current profile, and thus alter the equilibrium.

$$\frac{\partial \Delta'}{\partial t} = \frac{1}{\tau} \left(\Delta'_s(\rho_{RF}(t)) - \Delta' \right) \tag{15}$$

This model is able to capture the hysteresis phenomenon, as shown on figure 6.

Finally, one can wonder how less-efficient is the sweeping compared to the continuous deposition on the resonant surface for preempting. On figure 7, we have plotted the ability of the sweeping to preempt the $(2, 1)$-mode in presence of a sweep of given frequency $f = 4$ Hz, for different amplitudes and RF current intensity. Increasing the sweeping amplitude leads to a reduction of the operational domain of the preemption, since the excursion in the destabilizing regions lead to higher mode destabilization, in accordance with figure 4.

4 Mitigating radial misalignment issues in presence of an island

Similarly to the preemption case, in presence of an island, it is well known that radial misalignment can seriously reduce the control efficiency, or even lead to

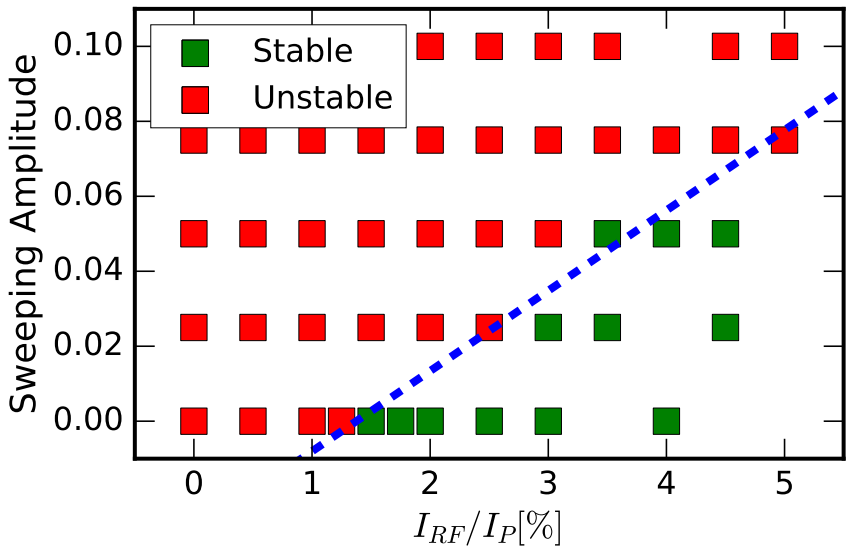

Figure 7: Ability of the sweeping to preempt the (2,1) mode $\gamma_{(2,1)}$. Green squares correspond to configurations where the mode is effectively preempted, while red squares correspond to configurations where preemption failed.

a destabilization of the mode, as seen for instance on JT-60U Isayama et al. (2000) or DIII-D Haye et al. (2002). This results can also be retrieved analytically by computing η_{RF} as a function of misalignment, calculations that show the decrease of η_{RF} as the misalignment is increased, as well as the existence of negative-η_{RF} areas (that is, destabilizing regions), which indicates that in some cases, misaligned ECCD is destabilizing Lazzari and Westerhof (2011); Février et al. (2016). Furthermore, this efficiency reduction with misalignment is dependent on the current deposition characteristics, thinner depositions leading to a larger decrease rate of η_{RF} with misalignment, as well as an increase of the destabilizing effect. Because of this sensitivity of η_{RF} (ρ_{RF}) to alignment, it is therefore necessary to be able to target as precisely as possible the exact radial location of the O-Point. In ITER, the maximum acceptable misalignment is expected to be about 2 cm Haye et al. (2008). However, beyond uncertainties on equilibrium reconstruction, knowledge of the mode position is complex to obtain and will also evolve during the stabilization of the mode, for instance due to the recovery of a larger Shafranov shift after the island stabilization. One of the possibilities to avoid this pitfall is to use a feedback control system that corrects the deposition location in real-time based on mode response. This is however complicated to achieve in practice, and a simpler, thus more robust, solution has been investigated in TCV Felici et al. (2012) or AUG Maraschek et al. (2015), where the radial position of the ECCD deposition is swept around the rational flux surface estimated position, ensuring that the current deposition will cross the magnetic island O-Point at least once in a while. On figure 8 we have plotted the evolution of a (2,1) magnetic island dynamics for continuous

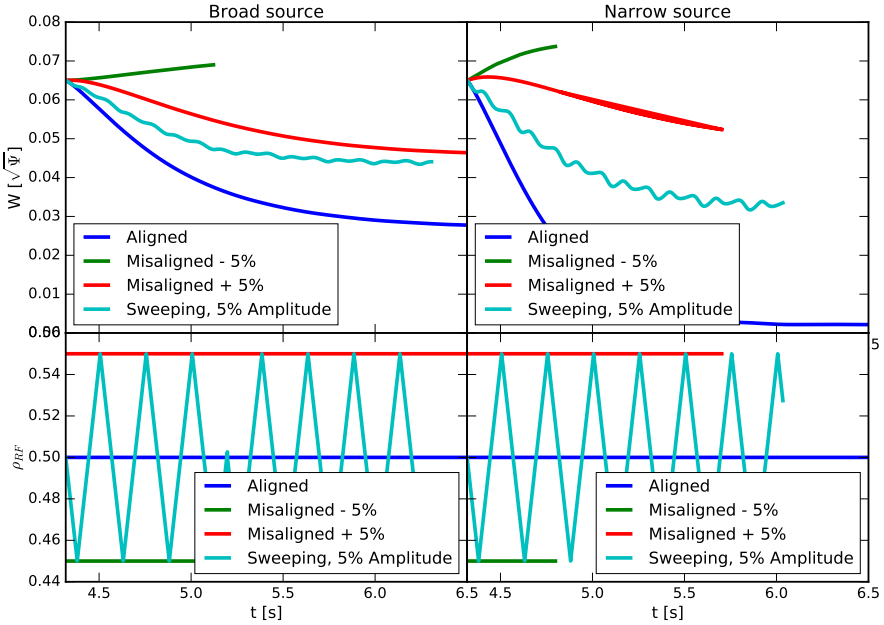

Figure 8: Evolution of the island width (top) and RF deposition location (bottom), for different source widths (broad source $\delta_{RF} \approx 1.4 W_{sat}$, left; thin source $\delta_{RF} \approx 0.7 W_{sat}$, right), different misalignments and with a sweeping centered on the resonance, at a frequency $f = 4$ Hz.

deposition, both aligned and misaligned, as well as for a swept deposition, for both a large and thin source. One can see that, in case of a misaligned deposition, the island is either further destabilized when depositing current inside the resonant surface, or stabilized with a lower efficiency when deposited outside, the destabilization being stronger in the case of a thin current deposition, which is in good agreement with both experimental observations and analytical computations. Sweeping the deposition around the rational surface enhances the stabilizing effect, and brings the island to a lower size even if scanning a large area around the resonance. One can now wonder if it is possible to optimize the sweeping process. Several levers appear to be available:

- The frequency of the sweeping, that will however be limited by the maximum angular velocity of the EC mirrors.
- The amplitude of the excursions around the rational surface.
- The position of the sweep mean value with respect to the estimated position of the rational surface.

4.1 Sweep frequency impact

On figure 9, we have plotted the resulting island dynamics for several values of the sweep frequency, in a range that is experimentally relevant. We note that for these values, the velocity of the sweeping does not impact the saturation size of

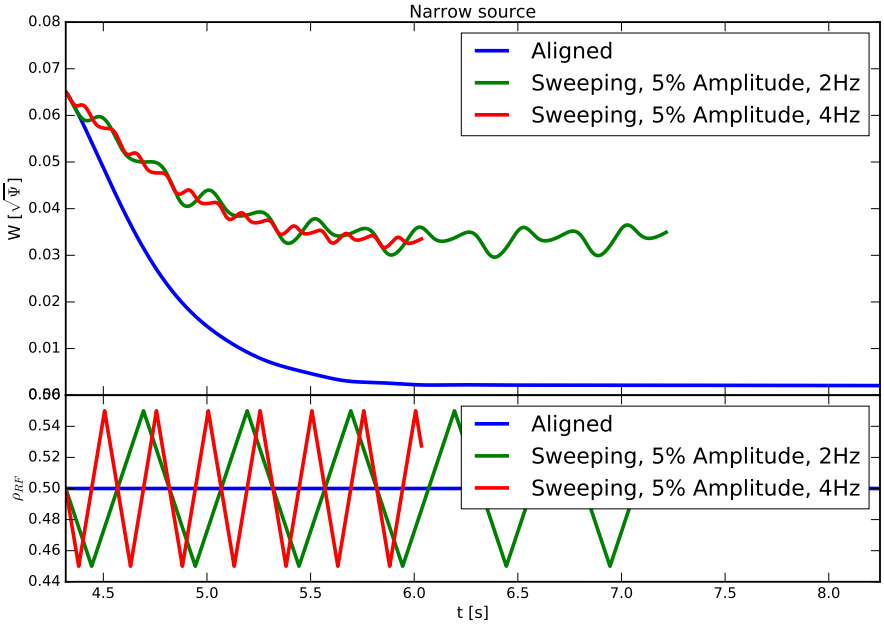

Figure 9: Evolution of the island width (top) and RF deposition location (bottom) for different sweeping frequencies.

the controlled island. Its dynamics is slightly different as slower sweeps allow for larger excursion of the mode size. This result makes sense as we are looking to a mean effect. With higher frequency, the position of the island is crossed more often, but less time is spent there. In the slow frequency limit ($f_{sweep} \to 0$), the sweep reproduces the behavior of a fixed source term placed on the sweep initial position, that is, potentially inefficient or destabilizing. Therefore, the sweeping frequency appears as a secondary parameter for optimization as it does not seem to play a significant role in the island dynamics, although one could expect uncertainty on the result if the sweep period is reduced well below the timescale of the mode evolution.

4.2 Sweeping amplitude and mean value impact

The influence of the sweeping amplitude and mean location is illustrated on figure 10, where we have plotted the saturation width of the controlled island as a function of the sweep amplitude and mean location with respect to the rational surface (denoted Δ_ρ^0 in the following) As expected, smaller oscillations around the position of the resonant surface (that is, no misalignment) are more efficient, as more time is spent in the vicinity of the island. On figure 10, we also have superimposed the results obtained for a misaligned sweep, whose mean location is not on the resonant surface, but 5% outside. One can see that the outwards-shifted sweep can be more efficient for a large sweep amplitude, which can be explained by considering the convolution of the asymmetric (with respect to the resonance) radial shape of η_{RF} with the sweep trajectory, the RF current

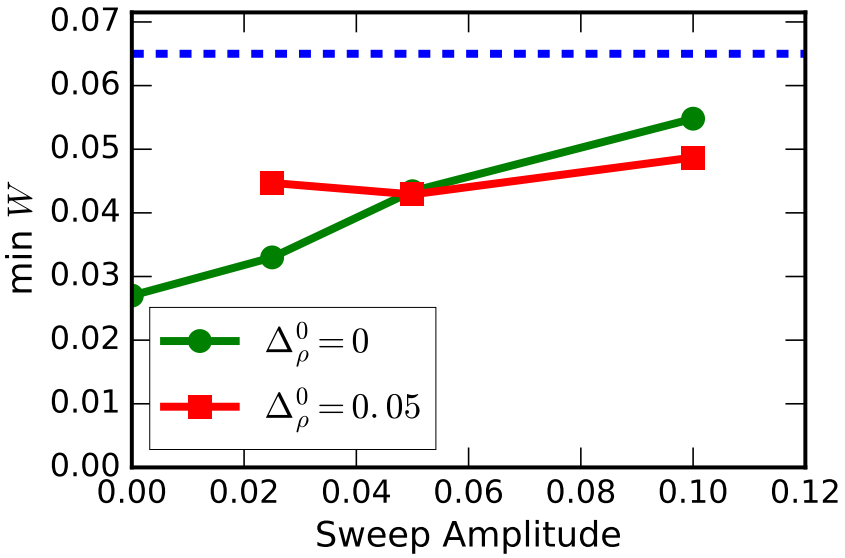

Figure 10: Saturation width reached as a function of sweeping amplitudes, for different misalignment of the sweeping. The dash line indicates the saturated width of the island.

being known to be destabilizing when deposited near the island separatrix, the destabilization being stronger in the inside of the resonant surface Lazzari and Westerhof (2011); Février et al. (2016). In order to illustrate this phenomenon, we use a simple shape for η_{RF} variation with misalignment, that we write as

$$\eta_{RF} \propto \left(1 - \left(\frac{\Delta\rho_{RF}}{\alpha}\right)^2\right) \exp\left(-\left(\frac{\Delta\rho_{RF}}{\beta}\right)^2\right) \tag{16}$$

where $\Delta\rho_{RF}$ is the misalignment and α and β being typical length scale quantify scale on which the efficiency decreases with misalignment as well as importance of destabilization when misaligned enough to target the island separatrix. This analytic formulation covers the destabilizing regions that are close to the island separatrix, but does not capture the radial asymmetry. We have plotted equation 16 on figure 11, with $\alpha = 0.037$ and $\beta = 0.039$. Based on figure 11, or numerical computations of efficiency such as in Lazzari and Westerhof (2011); Février et al. (2016), the results from figure 10 can be explained by the existence of two regions of negative efficiency for certain misalignments. If the misalignment of the deposition is such that the mean location of the sweeping lies in one of these regions, sweeping with too narrow an amplitude will confine the deposition in this area, hence resulting in, at best, a very poor efficiency and, at worst, a destabilization. Increasing the sweeping amplitude allows regions of positive efficiency to be accessed, thus enhancing the stabilization. This explains why, on figure 10, the misaligned sweep performs better with an amplitude $A = 0.05$ than with a lower amplitude of 0.025. The existence of two regions, one on each side of the resonance, also plays a role. When perfectly aligned, a sweep with a

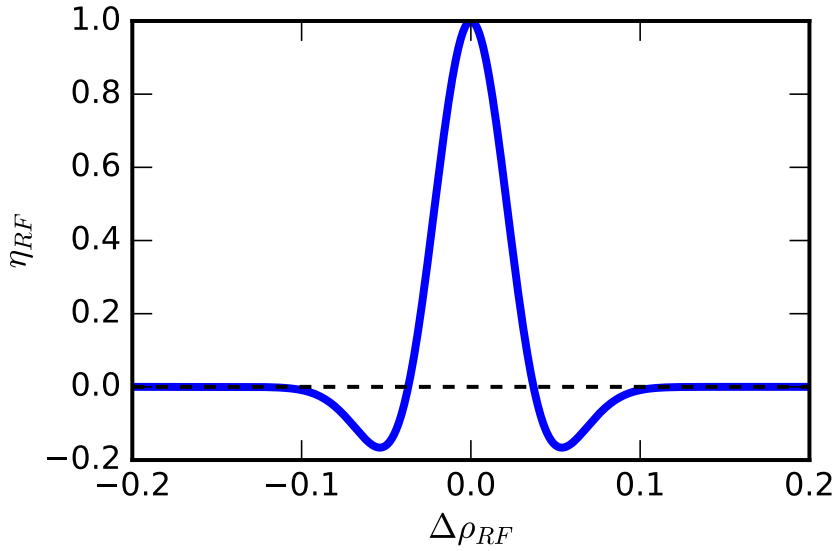

Figure 11: Efficiency η_{RF}, as approximated by equation 16, with $\alpha = 0.037$ and $\beta = 0.039$.

sufficiently large amplitude will explore these two destabilizing region, while a sweep slightly misaligned in one direction might explore only one of those, hence enhancing its efficiency. This explains why at the same amplitude $A = 0.1$, the misaligned sweep performs better than the aligned one. It should be noted that in our model, the efficiency is taken to be symmetric with respect to the resonance, which is not necessary the case in reality. Simulations wit XTOR-2F have indeed shown that the destabilization is stronger when misaligned inside the surface Février et al. (2016). Thus, a sweep misaligned in the inside of the rational surface might actually end up more destabilizing than a perfectly aligned one. A similar behavior can be observed when plotting the (anti)-correlation coefficient $R_J\,(J_{RF})$ as a function of the source radial position during a sweep, as done in figure 12 for two sweeping amplitudes. For both sweeps, one can see that the correlation is stronger when in the vicinity of the resonant surface, and drops as the source is moved away from the island. The asymmetry between inside and outside the resonant surface is clearly visible : while misalignment outside the resonant surface tends to reduce the correlation to zero, so that the source does not impact the island dynamics anymore, the misalignment inside tends to reduce the correlation below zero, leading to further mode destabilization. Furthermore, one can see that in the case of the lower-amplitude sweep, the correlation decreases along time. This is due to the reduction of the island width, leading to an increase of δ_I/W, and therefore, more-and-more current is deposited outside the island : the stabilization tends to be less efficient, hence the reduction of the correlation. This effect is not seen in the case of the larger sweep as it is already very-inefficient, and therefore, the island width does not drop as much as in previous case.

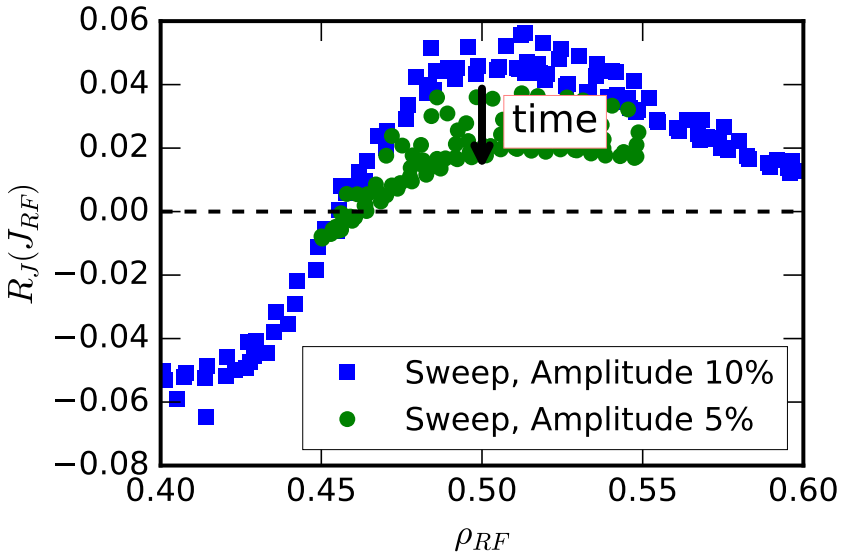

Figure 12: (Anti)-Correlation $R_J\left(J_{RF}\right)$ plotted for two sweeping amplitude control methods, in the case of the broad source term ($\delta_{RF} \approx 1.4 W_{sat}$). The correlation is stronger when in the vicinity of the resonance surface, and drops as the source is moved away from the island. The asymmetry between inside and outside the resonant surface is visible, and misalignment outside the resonant surface tends to reduce the correlation to zero, while misalignment inside tends to reduce the correlation below zero, leading to further mode destabilization. Furthermore, one can see that in the case of the lower-amplitude sweep, the correlation decreases along time, due to the diminution of the island width W, that is more pronounced than in the case of the larger sweep.

The loss of efficiency due to the sweeping process can be coarsely estimated by averaging the efficiency η_{RF} over a sweep period, leading to an effective efficiency factor η_{RF}^{sweep}:

$$\eta_{RF}^{sweep} = \frac{1}{T}\int_0^T \eta_{RF}\left(\rho_{RF}(t)\right)\mathrm{d}t \tag{17}$$

We consider a sweep of amplitude A and systematic misalignment of Δ_ρ^0, so that $\Delta\rho_{RF}(t) = \Delta_\rho^0 + A \times \text{triangle}\,(t)$, where triangle is the triangle function, ranging from -0.5 to 0.5. Neglecting the variation of the island width over a period (so that the formula is mostly valid at saturation), one can find an *effective efficiency* $\eta_{RF}^{eff} = \eta_{RF} \times \eta_{RF}^{sweep}$, where η_{RF} is the efficiency associated with a non-sweeping source term and η_{RF}^{sweep} a factor describing the efficiency modification by the sweeping process. Its computations from equations 17 and 16 gives

$$\begin{aligned}
\eta_{RF}^{sweep} &= \frac{1}{4}\frac{\beta}{\alpha^2 A}\left[2\sqrt{\pi}\alpha^2\mathrm{erf}\left(\frac{1}{2}\frac{A-2\Delta_\rho^0}{\beta}\right) + 2\sqrt{\pi}\alpha^2\mathrm{erf}\left(\frac{1}{2}\frac{A+2\Delta_\rho^0}{\beta}\right)\right.\\
&+ \beta A\mathrm{e}^{-\frac{1}{4}\frac{\left(A-2\Delta_\rho^0\right)^2}{\beta^2}} + \beta A\mathrm{e}^{-\frac{1}{4}\frac{\left(A+2\Delta_\rho^0\right)^2}{\beta^2}}\\
&+ 2\beta\Delta_\rho^0\mathrm{e}^{-\frac{1}{4}\frac{\left(A+2\Delta_\rho^0\right)^2}{\beta^2}} - 2\beta\Delta_\rho^0\mathrm{e}^{-\frac{1}{4}\frac{\left(A-2\Delta_\rho^0\right)^2}{\beta^2}}\\
&- \left.\sqrt{\pi}\beta^2\mathrm{erf}\left(\frac{1}{2}\frac{A-2\Delta_\rho^0}{\beta}\right) - \sqrt{\pi}\beta^2\mathrm{erf}\left(\frac{1}{2}\frac{A+2\Delta_\rho^0}{\beta}\right)\right]
\end{aligned} \tag{18}$$

Equation 18 is plotted on figure 13 for different values of the systematic misalignment Δ_ρ^0 and of the amplitude A, with $\alpha = 0.035$ and $\beta = 0.035$. One can see that the efficiency decreases as the systematic misalignment or the amplitude increase, but in the case of a large systematic misalignment, increasing the sweeping amplitude might allow to recover some efficiency, which is consistent with results obtained on figure 10. Finally, we should add that there might also be a possible role (albeit small) of a Δ' effect, which is known to be stabilizing outside the resonance and destabilizing inside Pletzer and Perkins (1999).

5 Mitigating current deposition width issues

The lack of control of the current deposition width requires the ability to increase the stabilization efficiency even in the case of a large source. This can be achieved using the modulation method, where the gyrotrons are turned on/off so that the RF current is deposited only at the O-point, thus leading to an increase of the efficiency in comparison with a continuous deposition. On figure 14, results from simulations using the simple controller described in section 2.2 are shown for both a thin source and a broader deposition. While the modulation is not clearly beneficial in the case of a narrow current deposition, where a continuous source was actually already able to suppress the island, in the case of a larger deposition, modulation allows suppressing the islands while the continuous source was unable to do it. It should be noted that at some point, when the island has been sufficiently reduced, the control system, being

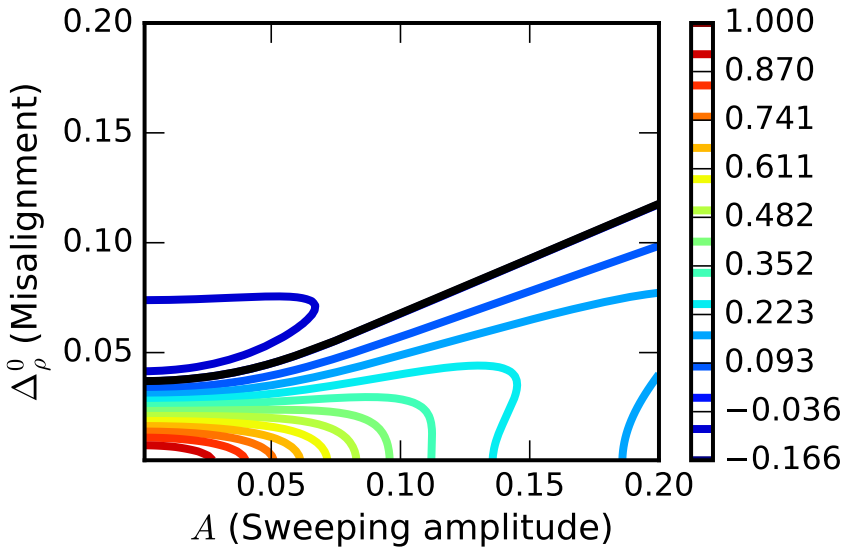

Figure 13: Effective efficiency factor η_{RF}^{sweep} as a function of sweeping amplitudes and systematic misalignment. The black curve seperates the domain of positive η_{RF}^{sweep} from the domain of negative η_{RF}^{sweep}.

coarsely implemented, is unable to properly detect the island phase and starts to behave erratically. In a proper (experimental) control system, a threshold mechanism shall be implemented to circumvent this issue. This process can be further improved by using advanced systems such as the FADIS (FAst DIrectional Switch) Kasparek et al. (2008), which allows switching the output of one gyrotron between two launchers, thus allowing island O-Point tracking, by setting the launchers so that when one is targeting the O-Point, the other one is targeting the X-Point. By detecting the phase of the island, and using the FADIS, it is therefore possible to direct the power towards the launcher that is targeting the island O-Point. Because of the island rotation, the O-Point will move away from the deposition location of this first launcher, and, in contrast with modulation where power is shutdown in this case, with FADIS, one only has to switch to the second launchers, that will be facing the O-Point, thus allowing a nearly continuous O-point hitting. This process is plotted on figure 14, and one can see that it yields a higher efficiency than modulation permits.

6 Integration of basic control schemes

In previous sections, we have presented nonlinear simulations allowing us to investigate control schemes that are able to mitigate radial positioning or width uncertainties. In this section, we summarize these results by introducing a gain function G defined as the value

$$G = \frac{W_{sat} - W_{min}}{W_{sat} - W_0} \tag{19}$$

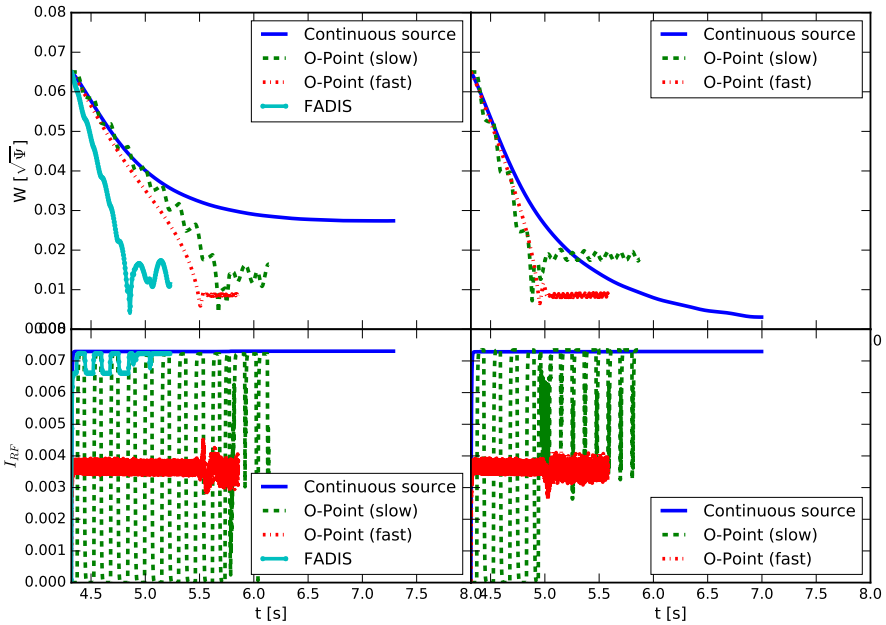

Figure 14: Evolutions of island width (top) and RF current (bottom) for a broad source ($\delta_{RF} \approx 1.4 W_{sat}$, left) and a thin source ($\delta_{RF} \approx 0.7 W_{sat}$, right) and for different control methods: a continuous source, and a 50% modulation with a slow rotation frequency ($f \approx 10$ Hz) and a faster one ($f \approx 1$ kHz).

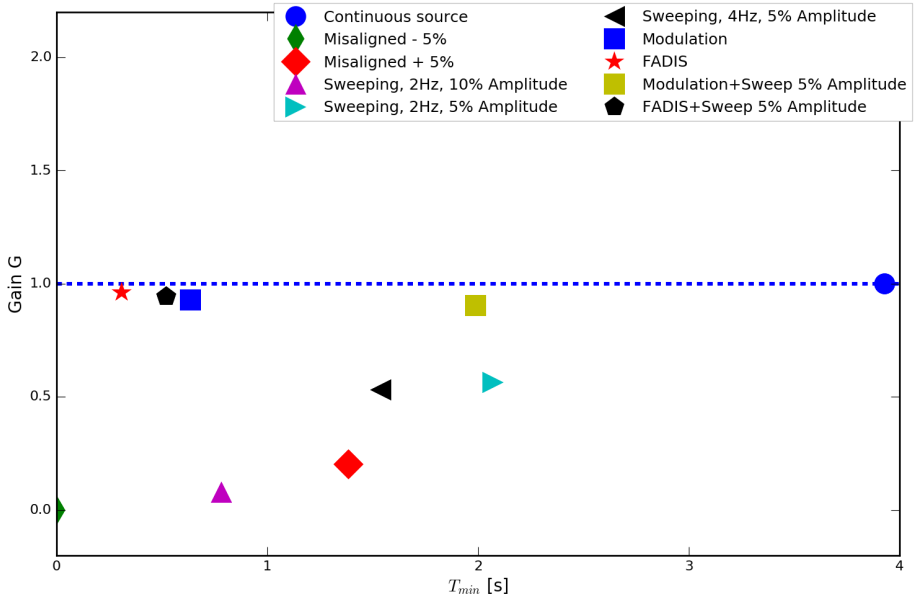

Figure 15: Gain function as a function of the time T_{min} necessary to reach the minimum island width, obtained with thin source term ($\delta_{RF} \approx 0.7 W_{sat}$). Notice how the sweeping allows increasing the gain with respect to a misaligned source, while being less efficient than a perfectly aligned source

where W_{sat} is the saturation width of the island, W_{min} the minimum width reached during the island control at $t = T_{min}$. For the continuous deposition, which tends towards asymptotic value W_0 (that, being asymptotic, would be reached only for $T_{min} = \infty$), we take T_{min} as the time needed to reach 95% of W_{min}. Note that in the case of a metastable mode (which is not the case here), control is achieved if at some point, the island width goes below a certain critical threshold $W_{critical}$, that corresponds to the critical width below which the island is unconditionally stable). W_0 is the minimum width that is reached with a perfectly aligned, continuous ECCD deposition. The gain is therefore unity for the fixed continuous source that is used as a reference, and it goes below (above) unity if the minimum island size is larger (lower) than this reference. On figures 15 and 16, we have plotted the gain of the different methods presented previously, both for the thin and broad source term, as a function of $t = T_{min}$, that is, the time necessary to reach the minimum width value. This is an important parameter, as an insufficiently fast reduction of the island width might give enough time for the island to lock van den Brand et al. (2012), bringing the plasma closer to disruption. Therefore, an ideal control mechanism should be able to reach a high G value in a minimum T_{min}. In the case of a thin source (figure 15), one can see the importance of the sweeping, which allows to mitigate the misalignment difficulty, while modulation or FADIS permits to reduce the island at a faster pace, although the minimal width stays the same. For the broad source (figure 16), the situation is different. While the sweeping still allows to regain a bit of efficiency (but not much when compared to an outside-misaligned sweep), the importance of modulation appears clearly, as the

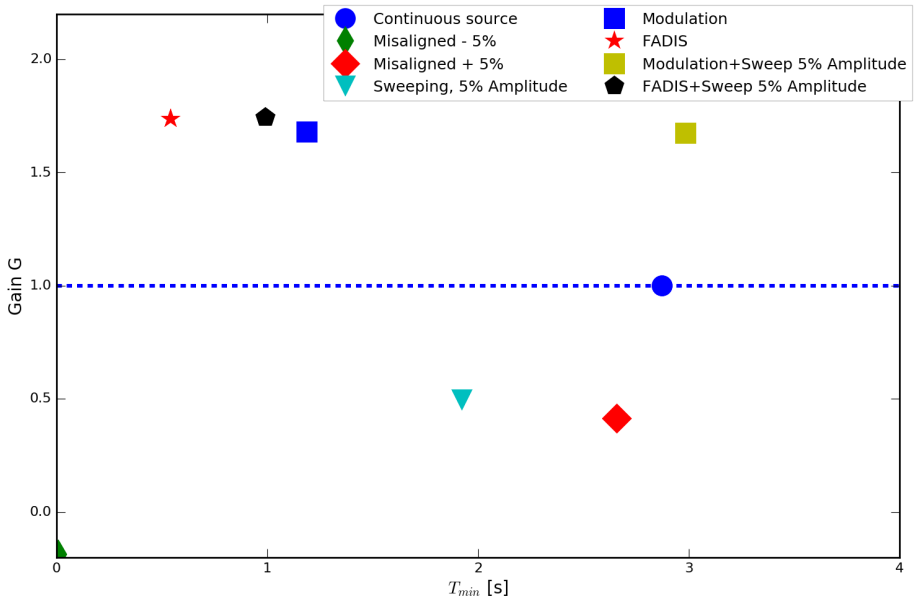

Figure 16: Gain function as a function of the time T_{min} necessary to reach the minimum island width, obtained with a broad source term ($\delta_{RF} \approx 1.4 W_{sat}$). While the sweeping does not change much the efficiency, the modulation allows to significantly enhance the stabilizing effect. Coupled with a sweeping, this provides a reliable method to control islands.

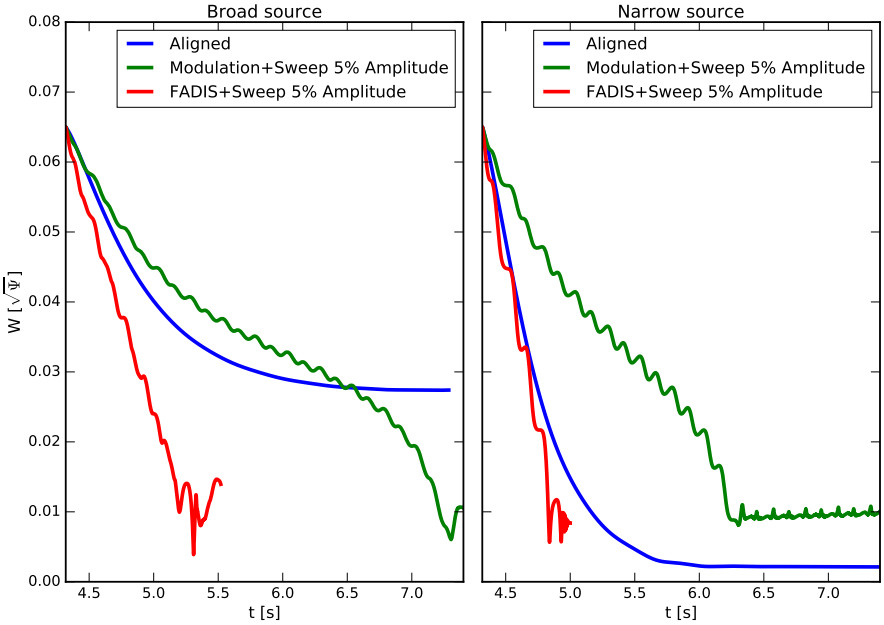

Figure 17: Evolution of island's width when controlled by a coupled method (Modulation + Sweep or FADIS + Sweep). In both case, the island can be suppressed or drastically reduced, proving that these schemes are good candidate for tokamak operations since they are robust towards misalignment or deposition width uncertainties.

minimum width of the island is almost divided by a factor two when modulating, in comparison with continuous deposition. Since modulation and sweeping process occur on different timescale -the modulation occurring on frequencies of a few kHz, while the sweeping frequency is limiting to a few Hz-, it should be possible to combine these two methods, thus achieving a control system that should, in principle, be both reliable with respect to the EC width and resonance position uncertainties. This is plotted on figure 17, both for the broad and thin deposition term. Interestingly, the combination of sweeping and modulation permits to completely suppress the mode in the case of the broad source term, the reduction of efficiency only having an impact on the stabilization time T_{min}. In the case of the thin EC deposition, the mode is also suppressed, in a fashion that allows robustness towards misalignment. Therefore, this appears as a very good candidate strategy for a tokamak operation, as this system is in principle robust towards both alignment and source width issues.

On figure 18, we have plotted the correlation coefficient R_J (J_{RF}) for the different control methods. On can clearly see that modulated methods (modulation or FADIS) are characterized by a higher overall (anti-)correlations, indicating that the current is more precisely deposited so as to counterbalance δJ_ϕ, which is of course the goal of aiming the O-Point. Continuous methods present excursions in the negative-values area, that is, the deposited current contributes to island reinforcement.

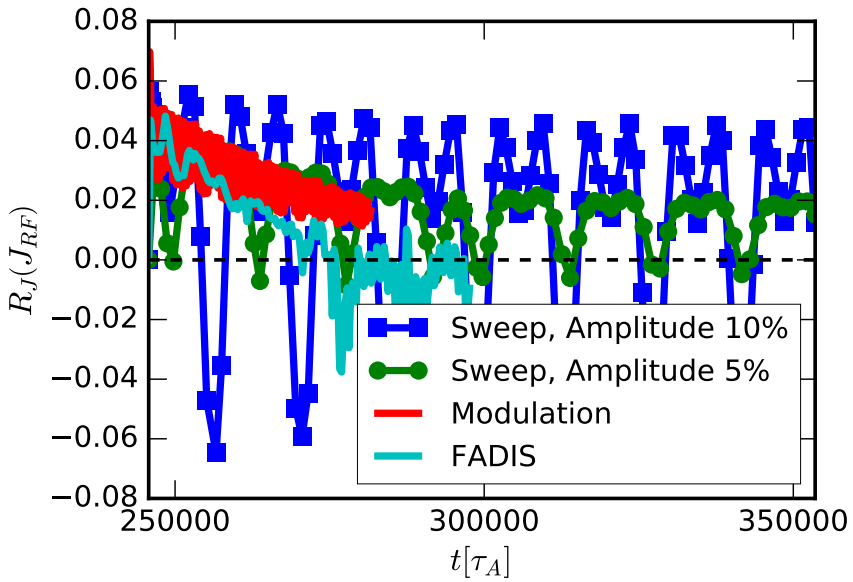

Figure 18: (Anti-)Correlation $R_J\,(J_{RF})$ plotted for different control methods, in the case of the broad source term ($\delta_{RF} \approx 1.4 W_{sat}$). One can see that modulated methods (modulation or FADIS) distinguish themselves by a higher overall correlation, indicating that the current is more precisely deposited so as to counterbalance δJ_ϕ, while continuous methods present excursions in the negative-values area, that is, the deposited current contributes to island reinforcement.

7 Conclusion

In this article, we have studied different possible stabilization strategies for island control in the framework of MHD simulations. In a first part, we have explored the preemption strategy, which consists in a preemptive strike to prevent the island apparition in the first place. We have shown that while MHD simulations in toroidal geometries give results in qualitative agreement with analytical results, a quantitative mismatch remains, our simulations showing a more abrupt transition from stabilization to destabilization than predicted in Pletzer and Perkins (1999). We then studied the different control strategy that can be used in order to control an existing island. It is well known that the characteristics of the current deposition are critical to ensure possible stabilization of the island. In particular, deposition broadness and alignment with rational surface are two key parameters defining the possibility to control a mode, technological or physical limitations might reduce the ability to fine-tune these parameters. We have compared different control strategies in the two cases of a current deposition larger or thinner than the island, defining a gain function that allows benchmarking the results from a particular strategy with the other and with the case of a continuous, perfectly aligned EC deposition, which constitutes the simplest case of island control, with however a high sensitivity to source broadness or misalignment issues. We have shown that each uncertainty (on deposition width or position) can be counterbalanced by the proper choice of strategy, that is, modulation in case of a large source or radial sweeping in case of radial misalignment. Furthermore, it appears possible to combine these strategies to form a robust control system.

8 Acknowledgement

The authors want to thank M. Reich and O. Sauter for useful discussions on control strategies. One of the author, O. Février, thanks C. Ehrlacher for assistance in the computation of equation 18 and R. Dumont for careful proofreading of this manuscript. This work is part of the AMICI project (ANR-14-CE32-0004-01) funded by the Agence Nationale pour la Recherche. Numerical resources were provided by CINES and TGCC of GENCI (x2015056348), Mésocentre of Aix-Marseille University (15b025), Helios of IFERC-CSC (MaCoToP).

References

Bertelli, N., Balakin, A., Westerhof, E., and Buyanova, M. (2010). ECCD calculations in ITER by means of the quasi-optical code. *Nuclear Fusion*, 50(11):115008, http://stacks.iop.org/0029-5515/50/i=11/a=115008.

Bertelli, N. and Westerhof, E. (2009). Consequences of finite transport on the effectiveness of ECCD for neoclassical tearing mode stabilization in ITER. *Nuclear Fusion*, 49(9):095018, http://stacks.iop.org/0029-5515/49/i=9/a=095018.

Casson, F., Poli, E., Angioni, C., Buchholz, R., and Peeters, A. (2015). Effect of turbulence on electron cyclotron current drive and heating in ITER. *Nu-*

clear Fusion, 55(1):012002, http://stacks.iop.org/0029-5515/55/i=1/a=012002.

Coda, S., Alberti, S., Blanchard, P., Goodman, T., Henderson, M., Nikkola, P., Peysson, Y., and Sauter, O. (2003). Electron cyclotron current drive and suprathermal electron dynamics in the TCV tokamak. *Nuclear Fusion*, 43(11):1361, http://stacks.iop.org/0029-5515/43/i=11/a=008.

Coda, S., Klimanov, I., Alberti, S., Arnoux, G., Blanchard, P., Fasoli, A., and the TCV team (2006). The effect of ECRH on the electron velocity distribution function. *Plasma Physics and Controlled Fusion*, 48(12B):B359, http://stacks.iop.org/0741-3335/48/i=12B/a=S33.

Decker, J., Peysson, Y., and Coda, S. (2012). Effect of density fluctuations on ECCD in ITER and TCV. *EPJ Web of Conferences*, 32:01016, DOI: 10.1051/epjconf/20123201016, http://dx.doi.org/10.1051/epjconf/20123201016.

Felici, F., Goodman, T., Sauter, O., Canal, G., Coda, S., Duval, B., Rossel, J., and the TCV Team (2012). Integrated real-time control of MHD instabilities using multi-beam ECRH/ECCD systems on TCV. *Nuclear Fusion*, 52(7):074001, http://stacks.iop.org/0029-5515/52/i=7/a=074001.

Février, O., Maget, P., Lütjens, H., Luciani, J. F., Decker, J., Giruzzi, G., Reich, M., Beyer, P., Lazzaro, E., Nowak, S., and the ASDEX Upgrade team (2016). First principles fluid modelling of magnetic island stabilization by electron cyclotron current drive (ECCD). *Plasma Physics and Controlled Fusion*, 58(4):045015, http://stacks.iop.org/0741-3335/58/i=4/a=045015.

Furth, H. P., Rutherford, P. H., and Selberg, H. (1973). Tearing mode in the cylindrical tokamak. *Physics of Fluids*, 16(7):1054–1063, DOI: 10.1063/1.1694467, http://link.aip.org/link/?PFL/16/1054/1.

Giruzzi, G. (1993). Modelling of RF current drive in the presence of radial diffusion. *Plasma Physics and Controlled Fusion*, 35(SA):A123, http://stacks.iop.org/0741-3335/35/i=SA/a=008.

Giruzzi, G. and Fidone, I. (1989). Impact of electron trapping on synchrotron radiation current drive. *Nuclear Fusion*, 29(12):2235, http://stacks.iop.org/0029-5515/29/i=12/a=015.

Glasser, A. H., Furth, H. P., and Rutherford, P. H. (1977). Stabilization of resistive kink modes in the tokamak. *Phys. Rev. Lett.*, 38:234–237, DOI: 10.1103/PhysRevLett.38.234, http://link.aps.org/doi/10.1103/PhysRevLett.38.234.

Glasser, A. H., Greene, J. M., and Johnson, J. L. (1975). Resistive instabilities in general toroidal plasma configurations. *Physics of Fluids*, 18(7):875–888, DOI: 10.1063/1.861224, http://link.aip.org/link/?PFL/18/875/1.

Hamamatsu, K. and Fukuyama, A. (2000). Numerical analysis of electron cyclotron current drive with suppressed Doppler broadening. *Plasma Physics and Controlled Fusion*, 42(12):1309, http://stacks.iop.org/0741-3335/42/i=12/a=306.

Harvey, R. W., Sauter, O., Prater, R., and Nikkola, P. (2002). Radial Transport and Electron-Cyclotron-Current Drive in the TCV and DIII-D Tokamaks. *Phys. Rev. Lett.*, 88:205001, DOI: 10.1103/PhysRevLett.88.205001, http://link.aps.org/doi/10.1103/PhysRevLett.88.205001.

Haye, R. J. L. (2006). Neoclassical tearing modes and their control. *Physics of Plasmas*, 13(5):055501, 055501, DOI: 10.1063/1.2180747, http://link.aip.org/link/?PHP/13/055501/1.

Haye, R. J. L., Günter, S., Humphreys, D. A., Lohr, J., Luce, T. C., Maraschek, M. E., Petty, C. C., Prater, R., Scoville, J. T., and Strait, E. J. (2002). Control of neoclassical tearing modes in DIII-D. volume 9, pages 2051–2060. AIP, DOI: 10.1063/1.1456066, http://link.aip.org/link/?PHP/9/2051/1.

Haye, R. L., Ferron, J., Humphreys, D., Luce, T., Petty, C., Prater, R., Strait, E., and Welander, A. (2008). Requirements for alignment of electron cyclotron current drive for neoclassical tearing mode stabilization in ITER. *Nuclear Fusion*, 48(5):054004, http://stacks.iop.org/0029-5515/48/i=5/a=054004.

Hegna, C. C. and Callen, J. D. (1997). On the stabilization of neoclassical magnetohydrodynamic tearing modes using localized current drive or heating. *Physics of Plasmas*, 4(8):2940–2946, DOI: 10.1063/1.872426, http://link.aip.org/link/?PHP/4/2940/1.

Isayama, A., Kamada, Y., Ide, S., Hamamatsu, K., Oikawa, T., Suzuki, T., Neyatani, Y., Ozeki, T., Ikeda, Y., Kajiwara, K., and the JT-60 team (2000). Complete stabilization of a tearing mode in steady state high-β_p H-mode discharges by the first harmonic electron cyclotron heating/current drive on JT-60U. *Plasma Physics and Controlled Fusion*, 42(12):L37–L45, http://stacks.iop.org/0741-3335/42/L37.

Kasparek, W., Petelin, M., Shchegolkov, D., Erckmann, V., Plaum, B., Bruschi, A., at IPP Greifswald, E. G., Karlsruhe, F., and Stuttgart, I. (2008). A fast switch, combiner and narrow-band filter for high-power millimetre wave beams. *Nuclear Fusion*, 48(5):054010, http://stacks.iop.org/0029-5515/48/i=5/a=054010.

Kirov, K. K., Leuterer, F., Pereverzev, G. V., Ryter, F., Suttrop, W., and team, A. U. (2002). ECRH power deposition studies in ASDEX Upgrade. *Plasma Physics and Controlled Fusion*, 44(12):2583, http://stacks.iop.org/0741-3335/44/i=12/a=307.

Kolemen, E., Welander, A., Haye, R. L., Eidietis, N., Humphreys, D., Lohr, J., Noraky, V., Penaflor, B., Prater, R., and Turco, F. (2014). State-of-the-art neoclassical tearing mode control in DIII-D using real-time steerable electron cyclotron current drive launchers. *Nuclear Fusion*, 54(7):073020, http://stacks.iop.org/0029-5515/54/i=7/a=073020.

Kotschenreuther, M., Hazeltine, R. D., and Morrison, P. J. (1985). Nonlinear dynamics of magnetic islands with curvature and pressure. *Physics of Fluids*, 28(1):294–302, DOI: 10.1063/1.865200, http://link.aip.org/link/?PFL/28/294/1.

Lazzari, D. D. and Westerhof, E. (2011). The role of asymmetries in the growth and suppression of neoclassical tearing modes. *Plasma Physics and Controlled Fusion*, 53(3):035020, http://stacks.iop.org/0741-3335/53/i=3/a=035020.

Lütjens, H., Bondeson, A., and Sauter, O. (1996). The CHEASE code for toroidal MHD equilibria. *Computer Physics Communications*, 97(3):219–260, http://www.sciencedirect.com/science/article/B6TJ5-3VSGD5T-19/2/e429c1260ed10db93fde0078b7cee3e6.

Lütjens, H. and Luciani, J.-F. (2010). XTOR-2F: A fully implicit Newton-Krylov solver applied to nonlinear 3D extended MHD in tokamaks. *Journal of Computational Physics*, 229(21):8130 – 8143, ISSN: 0021-9991, DOI: DOI:10.1016/j.jcp.2010.07.013, http://www.sciencedirect.com/science/article/B6WHY-50JPNF3-2/2/2787626de93153effa740cca124bcfe7.

Lütjens, H., Luciani, J.-F., and Garbet, X. (2001). Curvature effects on the dynamics of tearing modes in tokamaks. *Physics of Plasmas*, 8(10):4267–4270, http://link.aip.org/link/?PHP/8/4267/1.

Maraschek, M. (2012). Control of neoclassical tearing modes. *Nuclear Fusion*, 52(7):074007, http://stacks.iop.org/0029-5515/52/i=7/a=074007.

Maraschek, M., Reich, M., Behler, K., Giannone, L., Gude, A., Poli, E., Rapson, C., Sauter, O., Stober, J., Treutterer, W., H.Zohm, team, A. U., and team, E. M. (2015). Real-time control of mhd instabilities using eccd in asdex upgrade. 42th EPS Conference on Plasma Physics.

Peysson, Y., Decker, J., Morini, L., and Coda, S. (2011). RF current drive and plasma fluctuations. *Plasma Physics and Controlled Fusion*, 53(12):124028, http://stacks.iop.org/0741-3335/53/i=12/a=124028.

Pletzer, A. and Perkins, F. W. (1999). Stabilization of neoclassical tearing modes using a continuous localized current drive. *Physics of Plasmas*, 6(5):1589–1600, DOI: 10.1063/1.873412, http://link.aip.org/link/?PHP/6/1589/1.

Sauter, O. (2004). On the contribution of local current density to neoclassical tearing mode stabilization. *Physics of Plasmas*, 11(10):4808–4813, DOI: 10.1063/1.1787791, http://link.aip.org/link/?PHP/11/4808/1.

Sysoeva, E., da Silva, F., Gusakov, E., Heuraux, S., and Popov, A. (2015). Electron cyclotron resonance heating beam broadening in the edge turbulent plasma of fusion machines. *Nuclear Fusion*, 55(3):033016, http://stacks.iop.org/0029-5515/55/i=3/a=033016.

Tsironis, C., Peeters, A. G., Isliker, H., Strintzi, D., Chatziantonaki, I., and Vlahos, L. (2009). Electron-cyclotron wave scattering by edge density fluctuations in ITER. *Physics of Plasmas (1994-present)*, 16(11):–, 112510, DOI: http://dx.doi.org/10.1063/1.3264105, http://scitation.aip.org/content/aip/journal/pop/16/11/10.1063/1.3264105.

van den Brand, H., de Baar, M. R., Cardozo, N. J. L., and Westerhof, E. (2012). Integrated modelling of island growth, stabilization and mode locking: consequences for NTM control on ITER. *Plasma Physics and Controlled Fusion*, 54(9):094003, http://stacks.iop.org/0741-3335/54/i=9/a=094003.

Westerhof, E., de Blank, H., and Pratt, J. (2016). New insights into the generalized Rutherford equation for nonlinear neoclassical tearing mode growth from 2D reduced MHD simulations. *Nuclear Fusion*, 56(3):036016, http://stacks.iop.org/0029-5515/56/i=3/a=036016.